

Compound twin beams without the need of genuine photon-number-resolving detection

Jan Peřina Jr.,^{1,*} Antonín Černoch,¹ and Jan Soubusta²

¹Joint Laboratory of Optics of Palacký University and Institute of Physics of the Czech Academy of Sciences, Faculty of Science, Palacký University, 17. listopadu 12, 77146 Olomouc, Czech Republic

²Institute of Physics of the Czech Academy of Sciences, Joint Laboratory of Optics of Palacký University and Institute of Physics of CAS, 17. listopadu 50a, 772 07 Olomouc, Czech Republic

The scheme for building stronger multi-mode twin beams from a greater number of identical twin beams sufficiently weak so that single-photon sensitive on/off detectors suffice in their detection is studied. Statistical properties of these compound twin beams involving the non-classicality are analyzed for intensities up to hundreds of photon pairs. Their properties are compared with those of the genuine twin beams that require photon-number-resolving detectors in their experimental investigations. The use of such compound twin beams for the generation of sub-Poissonian light and measurement of absorption with sub-shot-noise precision is analyzed. A suitable theoretical model for the compound twin beams is developed to interpret the experimental data.

I. INTRODUCTION

In the history of detection of optical fields, two milestones occur. The first milestone was reached when the solid-state light detectors became sensitive enough to recognize individual detected photons (due to the used avalanche photodiodes (APDs) [1]). The second milestone is connected with the ability to count photons which is the basic method for characterizing optical fields [2, 3]. The first photon-number-resolving detectors (PNRDs) were simple: Two single-photon counting modules were used to monitor the outputs of a balanced beam splitter and resolve up to two photons. More complex geometries were applied [4] including the so-called fiber-loop PNRDs [5–7] with time multiplexing to extend the range of detected photons. Spatial multiplexing exploited in intensified CCD (iCCD) cameras [8, 9] and silicon matrix photodetectors [10] considerably enlarge the detectable photon numbers. Finally, genuine PNRDs based on super-conducting bolometers [11, 12] were constructed. In such PNRDs, the number of detected photons is linearly proportional to the energy absorbed and indirectly detected in super-conducting metallic wires [13].

The use of PNRDs in the investigation of nonclassical properties of optical fields including the entangled ones revealed various states with unusual physical properties: states with the reduced photon-number fluctuations (sub-Poissonian states [14], the Fock states as extreme examples), states containing only odd or even photon numbers [15, 16], states with perfect correlations in photon numbers [twin beams (TWBs)] [17], to name few. These states have found their application in metrology (absolute detector calibration [18–21], quantum imaging [22, 23] as well as sub-shot-noise measurements [24]). They have also been considered in quantum communica-

tions [25]. However, the PNRDs at present are complex and expensive devices and this limits the use of the above methods and applications.

This brings us to the question whether the PNRDs with their capabilities to detect optical fields can somehow be substituted by simpler APDs with their on/off detection, similarly as it is done in time and spatially multiplexed PNRDs. Such substitution is in principle possible for multi-mode optical fields that are composed of a greater number of spatial and spectral modes. When the mean numbers of photons in individual modes are considerably lower than one we may monitor the fields in individual modes by APDs. Provided that we are able to prepare the fields of individual modes independently, we can detect their properties by APDs mode by mode. Similarly as the whole optical field is built from individual modes its photon-number distribution is composed of the contributions from APDs that monitor individual modes. Whereas such approach is meaningless for the analysis of unknown optical fields, it is prospective for applications that use optical fields with well-defined properties, as mentioned above.

To demonstrate this approach, we consider TWBs and their application in quantum imaging. Several mean photon pairs per an imaged pixel are typically needed. The used TWB is typically composed of say N independent spatial modes and its statistical operator $\hat{\varrho}$ is written as a product of statistical operators $\hat{\varrho}_j$ of individual modes:

$$\hat{\varrho} = \prod_{j=1}^N \hat{\varrho}_j. \quad (1)$$

In the considered TWB, individual modes exhibit perfect photon pairing described by the thermal distribution with $b_{p,j}$ mean photon pairs,

$$\hat{\varrho}_j = \sum_{n_p=0}^{\infty} \frac{b_{p,j}^{n_p}}{(1 + b_{p,j})^{n_p+1}} |n_p\rangle_{s_j} |n_p\rangle_{i_j i_j} \langle n_p|_{i_j} \langle n_p|, \quad (2)$$

* jan.perina.jr@upol.cz

and the Fock state $|n_p\rangle_{s_j}$ ($|n_p\rangle_{i_j}$) contains n_p photons in the signal (idler) field of mode j . The mean photon-pair numbers $b_{p,j}$ of modes differ, but this has practically no influence on the properties exploited in the TWB applications. For this reason, we may substitute the TWB with statistical operator $\hat{\rho}$ in Eq. (1) by a TWB composed of N equally populated individual modes. Such TWB is described by the following statistical operator $\hat{\rho}^c$

$$\hat{\rho}^c = \hat{\rho}_{av}^{\oplus N} \quad (3)$$

in which the statistical operator $\hat{\rho}_{av}$ given by Eq. (2) contains $b_p = \sum_{j=1}^N b_{p,j}/N$ mean photon pairs. The TWB with statistical operator $\hat{\rho}^c$ in Eq. (3) is then suitable for practical realization in which we prepare N times the field with statistical operator $\hat{\rho}_{av}$. Thus, instead of measuring a stronger TWB given in Eq. (1) by two PNRDs, we measure N times a weak TWB with statistical operator $\hat{\rho}_{av}$ by two APDs and sum the results to arrive at those appropriate to a TWB given in Eq. (3). We call such TWBs the compound TWBs. The detection scheme is illustrated in Fig. 1 considering one of the beams that compose a TWB. We note that similar scheme was applied in the experimental study of non-Gaussian states in Ref. [26].

The compound TWBs generated in the substitution scheme are interesting on their own. Here, we demonstrate their usefulness when studying the behavior of TWB non-classicality for the intensities varying by three orders in magnitude. The substitution scheme assures close similarity of parameters of compound TWBs that differ in their intensities by orders in magnitude. Such analysis would not be possible for the usual experimental TWBs.

Sub-shot-noise imaging and quantum metrology represent the most important applications of stronger TWBs (composed of from several to several hundreds of photon pairs) at present. In one of their variants, they use sub-Poissonian fields as light sources for monitoring absorption coefficients of samples. They rely on the fact that the fluctuations in photon numbers in such fields are suppressed below the shot-noise-limit which allows to reach better measurement precision. Post-selection from a TWB [14, 27–29] whose one arm is monitored by a PNRD belongs to the most efficient methods of sub-Poissonian-light generation. Using the above discussed similarity of parameters of composed TWBs, we investigate the non-classicality of sub-Poissonian fields originating in the compound TWBs as it depends on the fields' intensity.

Finally, as the third example of the use of compound TWBs, we directly analyze the performance of compound TWBs in sub-shot-noise measurements [22, 24, 30, 31] by determining the precision of absorption measurements as it depends on the compound-TWB intensity. Such measurements were recently applied in microscopy [32, 33] and spectroscopy [34].

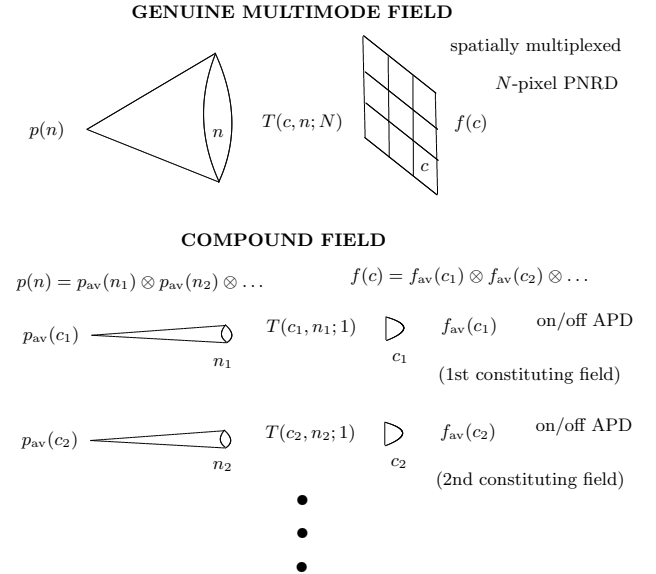


FIG. 1. Substitution scheme for a stronger multi-mode field with a photon-number distribution $p(n)$ detected by an N -pixel spatially multiplexed PNRD giving a photocount histogram $f(c)$. The stronger field is replaced by N identical weak fields with photon-number distributions $p_{av}(n)$ detected by APDs that provide photocount histograms $f_{av}(c)$. The photon-number distribution $p(n)$ and photocount histogram $f(c)$ are obtained by N -fold convolution from the photon-number distributions $p_{av}(n)$ and photocount histograms $f_{av}(c)$. The elements of detection matrix $T(c, n; N)$ give the probabilities of detecting c photocounts out of n impinging photons by an N -pixel detector.

We note that the use of APDs instead of genuine PNRDs in the discussed substitution scheme also benefits from considerably higher absolute detection efficiencies of APDs.

The paper is organized as follows. Photon-number as well as photocount distributions of genuine and compound TWBs are introduced in Sec. II. In Sec. III, the experiment is described and analyzed and the main characteristics of the generated fields are given. The determination of effective detection efficiency, which is an important parameter of PNRDs, is discussed in Sec. IV. Non-classicality of compound TWBs is analyzed in Sec. V using suitable non-classicality identifiers and the accompanying non-classicality depths. The generation of sub-Poissonian light by post-selection from compound TWBs is discussed in Sec. VI. Sub-shot-noise measurements of absorption coefficients using the compound TWBs are investigated in Sec. VII. Conclusions are drawn in Sec. VIII. In appendix, the model for describing the correlations in intra pump-pulse intensity fluctuations is developed.

II. PHOTON-NUMBER AND PHOTOCOUNT DISTRIBUTIONS OF GENUINE AND COMPOUND TWIN BEAMS.

The joint photon-number distribution $p_{\text{si}}(n_s, n_i)$ of an arbitrary TWB generated from parametric down-conversion can be described as a two-fold convolution of three photon-number distributions p_p , p_s and p_i belonging in turn to the paired, noise signal and noise idler components of the described TWB [35]:

$$p_{\text{si}}(n_s, n_i) = \sum_{n=0}^{\min(n_s, n_i)} p_s(n_s - n) p_i(n_i - n) p_p(n); \quad (4)$$

n_s (n_i) gives the number of signal (idler) photons. In the model, we assume the photon-number distributions of the components constituting the TWB in the form of the multi-mode thermal Mandel-Rice distribution [3] that is derived for a field with M_a equally populated modes and mean photon (-pair) number B_a per mode:

$$p_a(n; M_a, B_a) = \frac{\Gamma(n + M_a)}{n! \Gamma(M_a)} \frac{B_a^n}{(1 + B_a)^{n+M_a}}, \quad a = \text{s, i, p} \quad (5)$$

and Γ denotes the Γ -function.

The joint photocount distribution $f_{\text{si}}(c_s, c_i)$ [3] registered by two PNRDs composed of N_s and N_i equally illuminated pixels with on/off detection by the field with photon-number distribution $p_{\text{si}}(n_s, n_i)$ given in Eq. (4) is given as follows:

$$f_{\text{si}}(c_s, c_i) = \sum_{n_s, n_i=0}^{\infty} T_s(c_s, n_s; N_s) T_i(c_i, n_i; N_i) p_{\text{si}}(n_s, n_i); \quad (6)$$

c_s [c_i] denotes the number of signal (idler) photocounts that denote the photoelectrons registered by a detector after the absorption of photons.

For a detector with quantum detection efficiency η_a , number N_a of pixels and mean dark count number per pixel D_a , the elements of detection matrices T_a , $a = \text{s, i}$, introduced in Eq. (6) are derived in the form [9]:

$$T_a(c_a, n_a; N_a) = \binom{N_a}{c_a} (1 - D_a)^{N_a} (1 - \eta_a)^{n_a} (-1)^{c_a} \times \sum_{l=0}^{c_a} \binom{c_a}{l} \frac{(-1)^l}{(1 - D_a)^l} \left(1 + \frac{l}{N_a} \frac{\eta_a}{1 - \eta_a}\right)^{n_a}. \quad (7)$$

The derivation of Eq. (7) shows that when the mean number of photons illuminating one pixel is much less than one, i.e. when we can neglect illumination of a pixel by more than one photon, the elements of detection matrix $T_a(c_a, n_a; N_a)$ in Eq. (7) can be written as composed of the elements of independent detection matrices $T_a(c_a, n_a; 1)$ characterizing the detection by individual pixels.

In the substitution scheme, we assume that a genuine stronger TWB is replaced by a compound TWB, i.e. an

ensemble of N identical constituting TWBs detected by on/off APDs such that the mean photon numbers of the genuine and compound TWBs are the same. Though the mean photon-pair numbers of the constituting TWBs are much less than one, we still have to consider their multi-mode structure (see the discussion below). Provided that we have m_a modes in a constituting TWB, the mean photon (-pair) numbers b_a per mode of a constituting TWB are given as $b_a = B_a M_a / (m_a N)$, $a = \text{s, i, p}$. The formula analogous to that in Eq. (4) gives us the corresponding joint signal-idler photon-number distribution $p_{\text{si}}^w(n_s, n_i)$ of a constituting TWB. The constituting TWBs are detected by two APDs whose operation is described by the elements of detection matrix T_a in Eq. (7) assuming $N_a = 1$, $a = \text{s, i}$. The joint photocount distribution $f_{\text{si}}^w(c_s, c_i)$ appropriate to one constituting TWB is given as:

$$f_{\text{si}}^w(c_s, c_i) = \sum_{n_s, n_i=0}^{\infty} T_s(c_s, n_s; 1) T_i(c_i, n_i; 1) p_{\text{si}}^w(n_s, n_i). \quad (8)$$

For a compound TWB formed by N constituting TWBs, the probability f_{si}^c of having c_s signal photocounts together with c_i idler photocounts is determined by the following multiple convolution

$$f_{\text{si}}^c(c_s, c_i; N) = \sum_{c_{s,1}, c_{i,1}=0}^1 \cdots \sum_{c_{s,N}, c_{i,N}=0}^1 \delta_{c_s, \sum_{j=1}^N c_{s,j}} \delta_{c_i, \sum_{j=1}^N c_{i,j}} \prod_{j=1}^N f_{\text{si}}^w(c_{s,j}, c_{i,j}) \quad (9)$$

in which δ stands for the Kronecker symbol.

In analogy to Eqs. (8) and (9), the probability $p_{c,i}^w(n_i; c_s)$ of having n_i idler photons conditioned by the detection of c_s signal photocounts in a constituting TWB is given as:

$$p_{c,i}^w(n_i; c_s) = \sum_{n_s=0}^{\infty} T_s(c_s, n_s; 1) p_{\text{si}}^w(n_s, n_i). \quad (10)$$

The conditional probability $p_{c,i}^c(n_i; c_s)$ of having n_i idler photons after detecting c_s signal photocounts in a compound TWB formed by N constituting TWBs is then expressed as:

$$p_{c,i}^c(n_i; c_s, N) = \sum_{c_{s,1}=0}^1 \cdots \sum_{c_{s,N}=0}^1 \delta_{c_s, \sum_{j=1}^N c_{s,j}} \sum_{n_{i,1}=0}^{n_i} \cdots \sum_{n_{i,N}=0}^{n_i} \delta_{n_i, \sum_{j=1}^N n_{i,j}} \prod_{j=1}^N p_{c,i}^w(n_{i,j}; c_{s,j}). \quad (11)$$

III. EXPERIMENTAL CHARACTERIZATION OF COMPOUND TWIN BEAMS

The properties of compound TWBs were experimentally investigated in the setup shown in Fig. 2. The

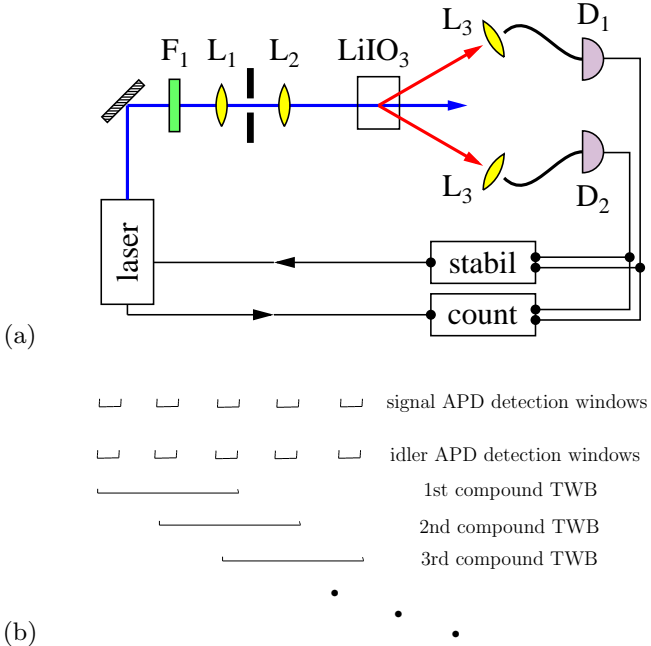


FIG. 2. (a) Experimental setup for generation of photon pairs in a nonlinear crystal LiIO_3 by short optical pulses and their detection by single-photon APDs D_1 and D_2 ; frequency filter F_1 and lenses $L_{1,2,3}$ transform the used beams. More details are written in the text. (b) Signal APD and idler APD detection windows and their grouping into triplets that give the measurement on compound TWBs formed by three constituting TWBs.

process of type-I parametric down-conversion in a LiIO_3 nonlinear crystal pumped by the third harmonic of an Nd-YAG laser at 355 nm and repetition rate 2.5 kHz was used to generate photon pairs with degenerate photon wavelengths centered at 710 nm. The laser was kept close above the threshold to give the power of only a few of mW. The third harmonic was spectrally cleaned by dichroic mirrors and 10-nm-wide spectral filter. To have the pump beam with an acceptable spatial profile in the nonlinear crystal we performed spatial filtering by a 4f system composed of two lenses (L_1 , L_2) with the focal lengths of 20 mm and 50 mm and the 50- μm -wide round aperture. The signal and idler photons were detected by single-photon APDs (Count-NIR from Laser Components) with nominal detection efficiencies about 80 % and very low dark count rates (< 50 Hz). Before being detected, the photons were spatially filtered by coupling into multi-mode fibers by means of lenses L_3 (15.3 mm focal length, 5 mm clear aperture). Electronic signals from the detectors were recorded simultaneously with the trigger from the laser using the counting logic electronics and directly sent to a computer for recording. Duration of pump pulses was 6.5 ns and similarly the signal and idler photons were emitted simultaneously in 6.5-ns-long time windows. Time delay between subsequent pulses was 4 ms. The detection events were recorded continuously and they formed two synchronized sequences of

on/off detections (in the signal and idler beams). The laser power was stabilized in a feed-back loop to keep stable operation of the experiment over tens of hours. Feedback was provided by monitoring the average single-photon detection rate during the measurement: Whenever the detection rate changed by more than 5 % the laser pump power was adjusted to compensate for this declination.

The analyzed experimental data represent a sequence of 695×10^6 measurements by single-photon APDs in individual detection windows (triggered by individual pump pulses) with the following four possible outcomes: no detection at both the signal and idler detectors, detection only at the signal detector, detection only at the idler detector or the coincidence detection at both detectors. An outcome in each detection window represents the measurement on one constituting TWB. Grouping of the outcomes in neighbor detection windows then gives us the information about compound TWBs. We have grouped the detections in N subsequent detection windows to arrive at the experimental photocount histogram $f_{\text{si}}^c(c_s, c_i; N)$ characterizing a compound TWB formed by N constituting TWBs. When forming the photocount histograms of compound TWBs, the outcomes in individual detection windows were multiply used following the scheme presented in Fig. 2(b).

The joint signal-idler photon-number distribution $p_{\text{si}}^c(n_s, n_i; N)$ of a compound TWB formed by N constituting TWBs has then been revealed using the reconstruction method based on the maximum-likelihood (ML) approach [36, 37]. It gives us the following iteration procedure for the reconstructed photon-number distribution p_{si}^c (j stands for the iteration index):

$$p_{\text{si}}^{c(j+1)}(n_s, n_i; N) = \sum_{c_s, c_i=0}^{\infty} F_{\text{si}}^{(j)}(c_s, c_i; N) T_s(c_s, n_s; N) \times T_i(c_i, n_i; N), \quad (12)$$

$$F_{\text{si}}^{(j)}(c_s, c_i; N) = f_{\text{si}}^c(c_s, c_i; N) \left[\sum_{n'_s, n'_i=0}^{\infty} T_s(c_s, n'_s; N) \times T_i(c_i, n'_i; N) p_{\text{si}}^{c(j)}(n'_s, n'_i; N) \right]^{-1}, \quad j = 0, 1, \dots$$

We characterize the obtained compound TWBs by their photocount (photon-number) moments $\langle c_s^k c_i^l \rangle$ ($\langle n_s^k n_i^l \rangle$) determined along the formula:

$$\langle c_s^k c_i^l \rangle = \sum_{c_s, c_i=0}^N c_s^k c_i^l f_{\text{si}}^c(c_s, c_i; N). \quad (13)$$

Fano factors $F_{c,a}$ ($F_{n,a}$) together with mean photocount (photon) numbers $\langle c_a \rangle$ ($\langle n_a \rangle$), $a = \text{s}, \text{i}$, defined in Eq. (13) are used to characterize the signal and idler marginal distributions:

$$F_{c,a} = \frac{\langle (\Delta c_a)^2 \rangle}{\langle c_a \rangle}, \quad (14)$$

$$\Delta c_a \equiv c_a - \langle c_a \rangle.$$

On the other hand, the noise-reduction-parameter R_c (R_n) and covariance C_c (C_n) of the photocount (photon) numbers c_s and c_i (n_s and n_i) are applied to quantify both quantum and classical correlations between the signal and idler fields:

$$R_c = \frac{\langle [\Delta(c_s - c_i)]^2 \rangle}{\langle c_s \rangle + \langle c_i \rangle}, \quad (15)$$

$$C_c = \frac{\langle c_s c_i \rangle}{\sqrt{\langle c_s^2 \rangle \langle c_i^2 \rangle}}. \quad (16)$$

The mean photocount numbers $\langle c_a \rangle$ as well as the corresponding mean photon numbers $\langle n_a \rangle$, $a = s, i$, of the marginal signal and idler fields of the compound experimental TWBs naturally increase linearly with the number N of constituting TWBs given by the number of grouped detection windows, as documented in Fig. 3(a). The Fano factors $F_{c,a}$ of the marginal experimental photocount histograms attain the values slightly smaller than 1 [for the idler Fano factor $F_{c,i}$, see Fig. 3(b)]. The values of Fano factors $F_{c,a}$, $a = s, i$, of the detected photocount histograms smaller than 1 originate in the pile-up effect [9, 10]. This effect occurs in the detection with a single-photon APD that allows to register up to one photocount. As the elements of detection matrix in Eq. (7) incorporates this effect, any reconstruction that uses these elements corrects for the pile-up effect. This is demonstrated in Fig. 3(b) where the values of the idler photon Fano factor $F_{n,i}$ are greater than 1, in agreement with the classical character of the marginal fields of compound TWBs. The photon Fano factors F_n of the marginal fields reconstructed by the ML approach systematically increase with the increasing number N of grouped detection windows. This behavior is observed also for the Fano factors F_c characterizing the photocount histograms, especially for the greater numbers N of grouped detection windows [Fig. 3(b)]. This increase is caused by weak temporal instability of the pump-pulse intensities that manifests themselves as correlations in intra pump-pulse intensity fluctuations. A stochastic model that describes this effect is developed in Appendix.

We compare the quantities characterizing both the experimental photocount histograms $f_{si}^c(c_s, c_i; N)$ and photon-number distributions $p_{si}^c(n_s, n_i; N)$ reconstructed by the ML approach with the predictions of two basic models. In the first model of a compound TWB, we assume that each detection window monitored by two APDs (one in the signal beam, the other in the idler beam) is illuminated by a Gaussian constituting TWB with $m_p = m_s = m_i = 10$ modes and mean photon (-pair) numbers per mode $b_p = 1.0185 \times 10^{-2}$, $b_s = 8 \times 10^{-5}$ and $b_i = 2 \times 10^{-5}$. We made the assumption $m_p = m_s = m_i$ for the numbers of modes of the (typical) constituting TWB and estimated the number m_p of modes in the dominant paired component of the constituting TWB from the reconstructed Fano factors F_{n_s} and F_{n_i} . Mean photon (-pair) numbers b_p , b_s and b_i were then set to accord with the mean photon numbers

$\langle n_s \rangle$ and $\langle n_i \rangle$ of the constituting TWB reconstructed by the ML approach. We note that the constituting TWB is practically noiseless (the unpaired noise photons comprise less than 1 % of the constituting TWB intensity). The second model is simpler. It assumes a genuine strong TWB having $M_a = N m_a$ modes each containing b_a mean photons or photon pairs, $a = p, s, i$ and its monitoring by two genuine PNRDs resolving up to N photons (N -pixel PNRDs).

The simpler second model of a genuine TWB detected by two N -pixel PNRDs with the photon-number distribution $p_{si}(n_s, n_i)$ given in Eq. (4) predicts the Fano factors F_n and F_c independent of the number N of detection pixels (windows) [see the dashed curves in Fig. 3(b)]. We arrive at nearly constant values of the photocount Fano factors F_c also when we apply the more elaborated first model of the compound TWB whose constituting TWBs are detected by APDs. The model is described by Eq. (9) that gives the solid curves in Fig. 3(b). The difference between two models is the following. In case of a genuine TWB and N -pixel PNRDs, each photon, independently on the mode in which it resides, can be detected by any pixel. It contrasts with the case of a compound TWB detected by APDs in which photons from a k -th constituting TWB can be detected only in the k -th detection window of the used APDs ($k = 1, \dots, N$). Thus, whereas the pile-up effect does not change with the increasing number N of detection windows of APDs in case of compound TWBs, it weakens with the increasing number N of detection pixels of PNRDs in case of genuine TWBs. Reduction of the pile-up effect in the latter case then results in the small increase of the artificially low values of the photocount Fano factors F_c with the increasing number N of pixels [see the dashed curve in Fig. 3(b)].

The comparison of the results of both models with the measured and reconstructed values of Fano factors F_c and F_n in Fig. 3(b) reveals the relatively strong influence of the above mentioned correlations in intra pump-pulse intensity fluctuations. The corresponding model presented in Appendix, that represents a suitable generalization of the first model, provides the solid plain curves in Fig. 3(b) that are in good agreement with the measured values. According to the model in Appendix, the greater the number N of grouped detection windows is, the greater the values of Fano factors F are. However, as the correlations in intra pump-pulse intensity fluctuations are specific to our experimental setup we refer to the model in Appendix only when needed.

On the other hand, correlations quantified by the photocount and photon noise-reduction-parameters R_c and R_n depend only weakly on the number N of grouped detection windows, as shown in Fig. 3(c). Whereas the values of photocount noise-reduction-parameters R_c are around 0.7 in agreement with the detection efficiencies of the used APDs, the values of noise-reduction-parameters R_n of the compound TWBs reconstructed by the ML approach are close to 0 indicating nearly ideal pairing of the signal and idler photons.

Covariances C_c and C_n of photocount and photon numbers, respectively, are plotted in Fig. 3(d). Whereas the covariances C_n of the reconstructed compound TWBs are close to the maximal allowed value 1 (excluding the TWB with $N = 1$ that is not suitable for ML reconstruction), the values of photocount covariances C_c gradually increase with the increasing number N of grouped detection windows. They are close to 1 for sufficiently great numbers N of grouped detection windows. This behavior follows from a simple model of N independent constituting TWBs each being described by the signal and idler photocount numbers $c_{s,j}$ and $c_{i,j}$, $j = 1, \dots, N$. The overall photocount numbers $c_a = \sum_{j=1}^N c_{a,j}$, $a = s, i$, then have the moments $\langle c_s c_i \rangle = N(N-1) \langle c_s \rangle^w \langle c_i \rangle^w + N \langle c_s c_i \rangle^w$ and $\langle c_a^2 \rangle = N(N-1) [\langle c_a \rangle^w]^2 + N \langle c_a^2 \rangle^w$, $a = s, i$, expressed in the moments of individual constituting TWBs $\langle c_a \rangle^w$, $\langle c_a^2 \rangle^w$, $a = s, i$, and $\langle c_s c_i \rangle^w$. Whereas we have $C_c = [\langle c_s c_i \rangle^w] / [\sqrt{\langle c_s^2 \rangle^w \langle c_i^2 \rangle^w}]$ for $N = 1$ constituting TWB, $C_c \rightarrow 1$ in the limit of large number N of constituting TWBs.

Intensities of the compound TWBs analyzed in Fig. 3 vary by three orders in magnitude: The weakest analyzed TWB formed by just one constituting TWB and detected in one detection window contains 0.102 mean photon pairs, the strongest compound TWB composed of 1000 constituting TWBs and thus detected in 1000 detection windows is composed of 102 photon pairs. Whereas the contribution of the vacuum state prevails in the weakest TWB, the joint photon-number distribution p_{si} of the strongest analyzed compound TWB exhibits a well developed pair-wise structure localized around the mean photon values [compare Figs. 4(a) and (b)]. These two types of photon-number distributions represent in certain sense the limiting cases of very weak TWBs (with mean photon-pair numbers much lower than 1) and stronger TWBs with their properties developed towards 'the classical limit' (mean photon-pair numbers in hundreds). Significant differences in their properties, as discussed below, originate in their joint quasi-distributions P_{si} of integrated intensities. We recall here that integrated intensities are introduced in the detection theory [3] in which the moments of integrated intensities refer to the normally-ordered photon-number moments. The quasi-distributions of integrated intensities for a given field-operator ordering parameter s are derived from the corresponding quasi-distributions of field amplitudes defined in the field phase space. The quasi-distributions of integrated intensities for s -ordered field operators can be determined from the corresponding joint photon-number distributions p_{si} along the formula [3]

$$P_{si,s}(W_s, W_i) = \frac{4}{(1-s)^2} \exp\left(-\frac{2(W_s + W_i)}{1-s}\right) \times \sum_{n_s, n_i=0}^{\infty} \frac{p_{si}(n_s, n_i)}{n_s! n_i!} \left(\frac{s+1}{s-1}\right)^{n_s+n_i} \times L_{n_s}\left(\frac{4W_s}{1-s^2}\right) L_{n_i}\left(\frac{4W_i}{1-s^2}\right) \quad (17)$$

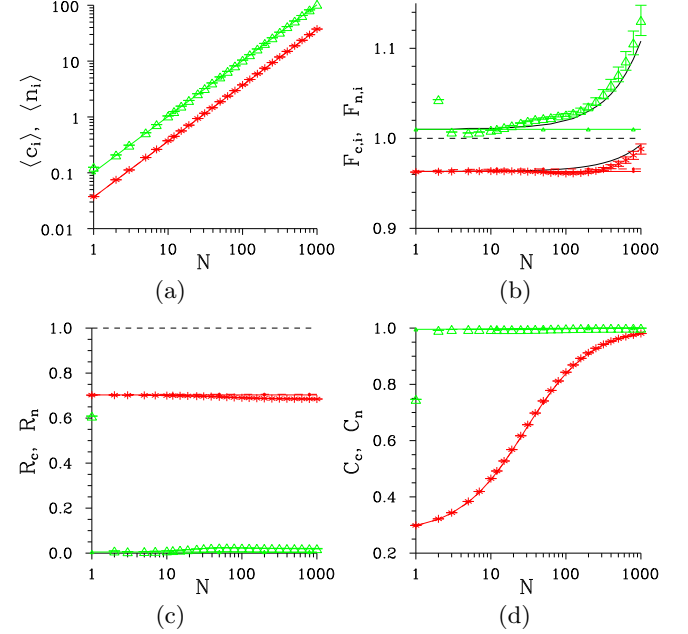


FIG. 3. (a) Mean number of photons $\langle n_i \rangle$ (photocounts $\langle c_i \rangle$) and (b) Fano factor $F_{n,i}$ (F_{c,i_1}) of the idler field, (c) noise-reduction-parameter R_n (R_c), and (d) covariance C_n (C_c) of the compound TWBs as they depend on the number N of grouped detection windows. Isolated symbols with error bars [in (a), (c) and (d) smaller than the plotted symbols] are drawn for the experimental photocount histograms (red $*$) and fields reconstructed by the ML approach (green Δ). Solid (dashed) curves with symbols originate in the model of compound (genuine) TWBs detected by APDs (N -pixel PNRDs). Black plain solid curves are drawn for the model of compound TWBs with correlations in intra pump-pulse intensity fluctuations. In (a), (c) and (d), the red solid and dashed curves nearly coincide. The horizontal plain dashed lines indicate the border between the classical and non-classical regions ($F = 1$, $R = 1$).

in which the symbol L_k denotes the k -th Laguerre polynomial [38]. In the quasi-distribution P_{si} of the weakest TWB plotted in Fig. 4(c), there occur local positive peaks and negative dips forming the structure with typical rays running from the beginning $(W_s, W_i) = (0, 0)$ and parabolas. On the other hand, the ray structure with the global positive maximum around the diagonal and negative 'valleys' sandwiched between positive local maxima characterize the quasi-distribution P_{si} of the strongest analyzed compound TWB plotted in Fig. 4(d). This reflects a well-formed pair-wise character of the compound TWB with 102 mean photon pairs.

IV. ANALYSIS OF EFFECTIVE DETECTION EFFICIENCY

Before we analyze the statistical properties of compound TWBs and their applications, we have to address first the effective detection efficiencies of PNRDs used in

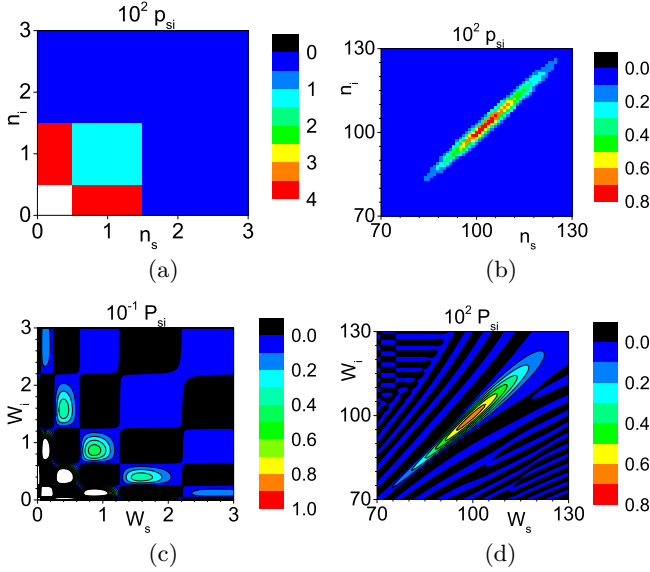


FIG. 4. (a,b) Photon-number distribution $p_{si}(n_s, n_i)$ and (c,d) the corresponding quasi-distribution $P_{si,s}(W_s, W_i)$ of integrated intensities for $N = 1$ [(a,c)] and $N = 1000$ [(b,d)]. In (c) [(d)], $s = 0.5$ [$s = 0$]. In (a) and (c), the values in white areas are greater than those explicitly indicated at the z scale.

TWB detection. The effective detection efficiency η^{eff} of a PNRD is an important parameter when experimental TWBs are analyzed. It arises from the generalization [20, 39] of the Klyshko method [18] for the determination of absolute detection efficiency developed originally for individual photon pairs. In fact it gives a refined effective value of the usual overall detection efficiency that involves in a real experiment the detector absolute quantum detection efficiency (estimated at 0.80 for the used APDs and appropriate wavelength) and losses on the way from the field source to the detector (dominantly caused by fiber coupling, estimated coupling efficiency below 0.35). This generalization suggests an appropriate effective detection efficiency η_s^{eff} of the signal detector in the form:

$$\eta_s^{\text{eff}} = \frac{\langle \Delta c_s \Delta c_i \rangle}{\langle c_i \rangle}. \quad (18)$$

The effective detection efficiency η^{eff} depends on TWB properties affected, among others, by the pump-pulse intensity fluctuations and TWB noises.

We first reveal the limitation of formula (18) by considering an intense genuine TWB described by the photon-number distribution p_{si} in Eq. (4). Assuming detection of such TWB by detectors with the detection efficiencies η_s and η_i and using the Mandel detection formula, the correlation function $\langle \Delta c_s \Delta c_i \rangle = \eta_s \eta_i (\langle \mathcal{W}_p \rangle + \langle (\Delta \mathcal{W}_p)^2 \rangle)$ [$\langle \mathcal{W}_a \rangle = M_a B_a$ for $a = p, s, i$, $\langle (\Delta \mathcal{W}_p)^2 \rangle = M_p B_p^2$], depends only on the paired component of the genuine TWB described by the integrated intensity \mathcal{W}_p [39]. On the other hand, the mean idler photocount number $\langle c_i \rangle = \eta_i [\langle \mathcal{W}_p \rangle + \langle \mathcal{W}_i \rangle]$ also depends on the noise

idler component with the integrated intensity \mathcal{W}_i . Under these conditions, the effective detection efficiency η_s^{eff} in Eq. (18) is derived in the form:

$$\eta_s^{\text{eff}} = \eta_s \frac{\langle \mathcal{W}_p \rangle + \langle (\Delta \mathcal{W}_p)^2 \rangle}{\langle \mathcal{W}_p \rangle + \langle \mathcal{W}_i \rangle}. \quad (19)$$

According to Eq. (19), if a TWB is noiseless [$\langle \mathcal{W}_i \rangle = 0$] and photon-pair statistics is Poissonian [$\langle (\Delta \mathcal{W}_p)^2 \rangle = 0$] [3], we directly have $\eta_s^{\text{eff}} = \eta_s$. Otherwise, the photon-pair number fluctuations exceeding the Poissonian ones increase the effective efficiency η_s^{eff} . The noise acts in the opposed way.

In the experiment, the effective signal- and idler-field detection efficiencies η_s^{eff} and η_i^{eff} are more-less constant for the number N of grouped detection windows up to 100 and then they gradually increase with the increasing number N [see Fig. 5(a)]. It follows from the curves in Fig. 5(a) that the subtraction of the known dark count rates $D_s = 2.8 \times 10^{-3}$ and $D_i = 3.8 \times 10^{-3}$ from the experimental mean photocount numbers $\langle c_a \rangle$ in Eq. (18) increases the effective detection efficiencies η_a^{eff} , $a = s, i$, by about 2 %. On the other hand, the values of the detection efficiencies $\eta_s = 0.282$ and $\eta_i = 0.330$ used in the theoretical fit of the experimental data in Fig. 5(a) are about 1 % greater than the measured effective detection efficiencies η^{eff} for $N \leq 100$. This is a consequence of little amount of the noise present in the experimental compound TWBs. According to the formula in Eq. (19), the theoretical effective detection efficiencies η^{eff} are independent of the number N of grouped detection windows as both expressions in the numerator and denominator are linearly proportional to the number N of grouped detection windows, as documented by the curves in Fig. 5(a). The effective detection efficiencies η^{eff} appropriate to N -pixel PNRDs behave very similarly, as it follows from the curves in Fig. 5(a). This behavior originates in the fact that the mean number of photons impinging on one detection pixel is considerably smaller than one. However, we note here that for small numbers m_p of paired modes in a constituting TWB (in one detection window), i.e. when the TWB photon-number distribution is close to the thermal one, the efficiencies η^{eff} slightly decrease for small numbers N . This effect is described by the term $\langle (\Delta \mathcal{W}_p)^2 \rangle$ in Eq. (19).

The increase of effective detection efficiencies η^{eff} for $N \geq 100$ is attributed to correlations in intra pump-pulse intensity fluctuations already observed in the graphs of the marginal Fano factors $F_{c,i}$ and $F_{n,i}$ in Fig. 3(b). To quantify these correlations, we determine the normalized correlation function $K_{a,\Delta j}$ of photocount fluctuations $\Delta c_{a,j}$ and $\Delta c_{a,j+\Delta j}$ of field a , $a = s, i$, mutually shifted by Δj detection windows for large number N_M of measurement repetitions:

$$K_{\Delta j} = N_M \frac{\sum_{j=1}^{N_M} \Delta c_{a,j} \Delta c_{a,j+\Delta j}}{\sum_{j=1}^{N_M} c_{a,j}}. \quad (20)$$

When processing the experimental data, the sum over

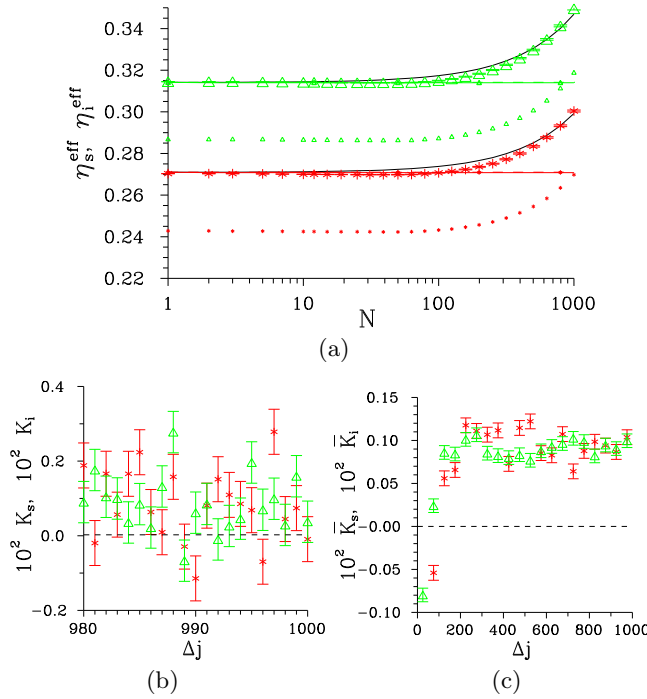


FIG. 5. (a) Effective detection efficiencies η^{eff} obtained with (large symbols) and without (small symbols) subtraction of the detector dark counts are plotted as functions of the number N of grouped detection windows. (b) Normalized photocount correlation functions K and (c) averaged normalized photocount correlation functions \bar{K} as they depend on the relative distance Δj of detection windows; $\bar{K}_{\Delta j} \equiv \sum_{\Delta k \in (\Delta j - \delta j, \Delta j + \delta j)} K_{\Delta k} / (2\delta j + 1)$. Experimental data are plotted as isolated symbols with error bars [in (a) smaller than the plotted symbols] for the signal (red, $*$) and idler (green, Δ) detectors. Solid (dashed) curves with symbols in (a) originate in the model of compound (genuine) TWBs detected by APDs (N -pixel PNRDs), the curves nearly coincide. Black plain solid curves in (a) are drawn for the model of compound TWBs with correlations in intra pump-pulse intensity fluctuations. The dashed horizontal lines in (b) and (c) indicate neutral correlations $K = \bar{K} = 0$; $\delta j = 24$.

index j runs over all detection windows. Random fluctuations of the normalized correlation functions K_s and K_i for $\Delta j \in \langle 980, 1000 \rangle$ are documented in Fig. 5(b). Despite the large relative distance Δj between the detection windows, they tend to exhibit positive correlations. The normalized correlation functions \bar{K}_s and \bar{K}_i averaged over 49 neighbor indices Δj and plotted in Fig. 5(c) clearly express positive correlations for Δj comparable or greater than 100. On the other hand, negative correlations are observed for Δj smaller than 100. They originate in the electronic response of the detector in general known as the death-time effect. The correlations quantified in the graphs of Figs. 5(b,c) provide suitable values of parameters of the model for correlations in intra pump-pulse intensity fluctuations and compound TWB generation developed in Appendix. The resultant curves for the effective detection efficiencies η^{eff} are drawn in Fig. 5(a)

by plain solid black curves.

V. NON-CLASSICALITY OF COMPOUND TWIN BEAMS

The most striking property of TWBs is their non-classicality that originates in tight correlations between the signal and idler photon numbers [8, 40–43]. As the marginal signal and idler beams are classical, the TWB non-classicality in fact reflects the entanglement (quantum correlations) between the signal and idler beams. We note that this entanglement is different from that usually discussed for individual photon pairs in quantum superposition states [2]. For compound TWBs, the amount of their overall noise increases linearly with the number of included constituting TWBs and so the question is to which extent the non-classicality is preserved for stronger compound TWBs. We show that the non-classicality of compound TWBs even increases with their intensity, owing to their increasing photon-pair number.

The non-classicality of TWBs is identified by non-classicality identities (NCIs), usually based on the non-classicality inequalities written either in (integrated) intensity moments [44] or containing the probabilities of photon-number (or photocount) distributions [45]. Here, we restrict our attention to the NCIs based on the intensity moments. The intensity moments $\langle W_s^k W_i^l \rangle$ are derived from the photon-number moments $\langle n_s^m n_i^j \rangle$ using the following formula

$$\langle W_s^k W_i^l \rangle = \sum_{m=0}^k S(k, m) \sum_{j=0}^l S(l, j) \langle n_s^m n_i^j \rangle \quad (21)$$

that includes the Stirling numbers S of the first kind [46]. We note that the relations in Eq. (21) between the normally-ordered photon-number moments (referred as intensity moments) and the usual photon-number moments originate in the canonical commutation relations. We also address the non-classicality of the directly detected photocount distributions f_{si}^c . To do this, we pretend as if the analyzed photocount distributions f_{si}^c were obtained by ideal detectors and determine the associated intensity moments $\langle W_s^k W_i^l \rangle_c$ from the photocount moments $\langle c_s^m c_i^j \rangle$ along the formula (21).

The intensity NCIs for TWBs were comprehensively analyzed in [44]. Our motivation here is twofold. First, to study the higher-order non-classicality indicated by higher-order intensity moments for the compound TWBs with the intensities varying over three orders in magnitude. Second, to identify the best performing NCIs, especially for greater numbers N of grouped detection windows. In our analysis, the following NCIs containing the intensity moments up to the fifth order were found the best [44]:

$$E_{001} \equiv \langle W_s^2 \rangle + \langle W_i^2 \rangle - 2\langle W_s W_i \rangle < 0, \quad (22)$$

$$E_{101} \equiv \langle W_s^3 \rangle + \langle W_s W_i^2 \rangle - 2\langle W_s^2 W_i \rangle < 0, \quad (23)$$

$$E_{111} \equiv \langle W_s^3 W_i \rangle + \langle W_s W_i^3 \rangle - 2 \langle W_s^2 W_i^2 \rangle < 0, \quad (24)$$

$$E_{211} \equiv \langle W_s^4 W_i \rangle + \langle W_s^2 W_i^3 \rangle - 2 \langle W_s^3 W_i^2 \rangle < 0. \quad (25)$$

Only the following two NCIs derived from the matrix approach were capable to indicate the non-classicality of the directly measured photocount distributions f_{si}^c for greater numbers N of grouped detection windows:

$$M_{1001} \equiv \langle W_s^2 \rangle \langle W_i^2 \rangle - \langle W_s W_i \rangle^2 < 0, \quad (26)$$

$$M_{001001} \equiv \langle W_s^2 \rangle \langle W_i^2 \rangle + 2 \langle W_s W_i \rangle \langle W_s \rangle \langle W_i \rangle - \langle W_s W_i \rangle^2 - \langle W_s^2 \rangle \langle W_i \rangle^2 - \langle W_s \rangle^2 \langle W_i^2 \rangle < 0. \quad (27)$$

The above NCIs can even be used for quantifying the non-classicality when the corresponding Lee non-classicality depths (NCD) [47] are determined. To do this, we first determine the intensity moments $\langle W_s^k W_i^l \rangle_s$ related to a general s ordering of the field operators from the normally-ordered intensity moments $\langle W_s^k W_i^l \rangle$ using the coefficients of the Laguerre polynomials L_k [3]:

$$\langle W_s^k W_i^l \rangle_s = \left(\frac{1-s}{2} \right)^{k+l} \left\langle L_k \left(\frac{2W_s}{s-1} \right) L_l \left(\frac{2W_i}{s-1} \right) \right\rangle. \quad (28)$$

Then we apply the above NCIs written directly for the s -ordered intensity moments $\langle W_s^k W_i^l \rangle_s$. The non-classicality indicated by the NCIs is gradually suppressed with the decreasing value of the ordering parameter s due to the increasing detection noise related to the operator ordering. Using this we look for the threshold value s_{th} at which a given NCI nullifies. It gives the border between the quantum and the classical behavior. The corresponding NCD τ is derived as follows [47]

$$\tau = \frac{1-s_{th}}{2}. \quad (29)$$

It gives the least mean number of thermal photons of a noisy field that, when superimposed on the analyzed field, guarantees the suppression of non-classicality of the analyzed field. It holds that $0 < \tau \leq 1/2$ for any non-classical 2D Gaussian field.

Whereas the NCIs E defined in Eqs. (22)–(25) identify the non-classicality for any reconstructed compound TWB, they fail to resolve the non-classicality directly contained in the corresponding photocount distributions f_{si}^c belonging to stronger compound TWBs (for $N \geq 800$), as documented by the curves of NCDs $\tau_{E,c}$ and $\tau_{E,n}$ in Figs. 6(a,b). This is a consequence of the noise present in TWB photocount distributions f_{si}^c whose level increases linearly with the number N of grouped detection windows. The reached values of NCDs $\tau_{E,c}$ and $\tau_{E,n}$ slightly decrease with the increasing order of the involved intensity moments. Nevertheless, the NCDs $\tau_{E,n}$ for the reconstructed compound TWBs tend to approach the values close to the maximal allowed value 1/2 for large numbers N of grouped detection windows. On the other hand, the maximal values of NCDs $\tau_{E,c}$ for the photocount distributions f_{si}^c close to 0.14 are reached for N around 50.

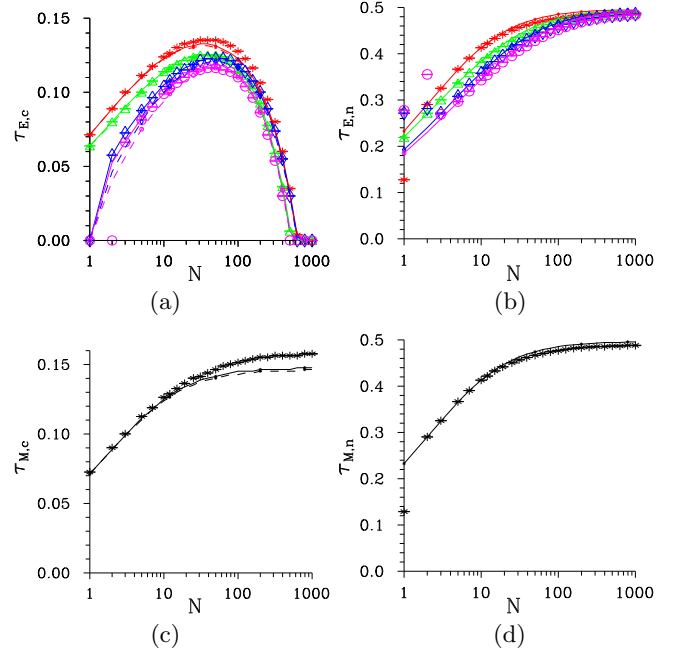


FIG. 6. Non-classicality depths for (a,c) the joint photocount (τ_c) and (b,d) the joint photon-number (τ_n) distributions as they depend on the number N of grouped detection windows. The NCIs E_{001} (red, $*$), E_{101} (green, Δ), E_{111} (blue, \diamond), and E_{211} (magenta, \circ) are used in (a,b), the NCI M_{1001} ($*$) is drawn in (c,d). Experimental data are plotted by isolated symbols, their error bars are smaller than the plotted symbols. Solid (dashed) curves originate in the model of compound (genuine) TWBs detected by APDs (N -pixel PNRDs); the solid and dashed curves nearly coincide.

The NCIs M written in Eqs. (26) and (27) reveal the non-classicality also for the photocount distributions f_{si}^c of strong composed TWBs, as shown in Fig. 6(c) for the NCI M_{1001} . Moreover, the obtained values of NCDs $\tau_{M,c}$ increase with the number N of grouped detection windows, similarly as those of NCDs $\tau_{M,n}$ appropriate for the reconstructed compound TWBs [Fig. 6(d)]. We note that the values of the NCDs τ_M belonging to the NCIs in Eqs. (26) and (27) are for the analyzed compound TWBs very close to each other independently of the number N . As the NCI M_{001001} in Eq. (27) has a more complex structure than the NCI M_{1001} in (26), it is more prone to the experimental errors. That is why we prefer to use the NCI M_{1001} for identification of the non-classicality of compound TWBs of arbitrary intensity. Both theoretical models for TWBs and their detection give good predictions for the NCDs τ derived from photon-number and photocount distributions, as it is shown in Fig. 6: The model of compound TWBs detected by APDs predicts slightly larger values of the NCDs τ for photocount distributions compared to the model of genuine TWBs detected by N -pixel PNRDs (stronger pile-up effect).

VI. SUB-POISSONIAN LIGHT GENERATION

Compound TWBs may also be used for efficient generation of sub-Poissonian light via post-selection. Post-selection by PNRDs applied to TWBs belongs, together with the cavity quantum electrodynamics schemes [48], to the most efficient methods of sub-Poissonian-light generation with greater photon numbers, both in cw [27, 28, 49] and pulsed regimes [11, 29, 41, 50, 51]. However, for realistic PNRDs, the method gradually loses its potential with the increasing post-selecting photocount number which limits the maximal intensities of the generated sub-Poissonian fields. Here, we address this limitation for compound TWBs and APDs.

An idler field conditioned by the detection of c_s signal photocounts is experimentally characterized by the conditional photocount histogram $f_{c,i}^c(c_i; c_s)$ derived from the joint signal-idler photocount histogram $f_{si}^c(c_s, c_i)$ by appropriate normalization:

$$f_{c,i}^c(c_i; c_s) = \frac{f_{si}^c(c_s, c_i)}{\sum_{c'_i=0}^{\infty} f_{si}^c(c_s, c'_i)}. \quad (30)$$

The corresponding conditional idler photon-number distributions $p_{c,i}^c(n_i; c_s)$ can then be obtained using the ML approach, similarly as in the case of TWBs. The looked-for distribution $p_{c,i}^c(n_i; c_s, N)$ obtained from a compound TWB formed by N constituting TWBs (detected in N detection windows of APDs) is found as a steady state of the following iteration procedure (j stands for the iteration index):

$$p_{c,i}^{c(j+1)}(n_i; c_s, N) = \sum_{c_i=0}^{\infty} F_i^{(j)}(c_i; c_s, N) T_i(c_i, n_i; N), \quad (31)$$

$$F_i^{(j)}(c_i; c_s, N) = f_{c,i}^c(c_i; c_s, N) \left[\sum_{n'_i=0}^{\infty} T_i(c_i, n'_i; N) \times p_{c,i}^{c(j)}(n'_i; c_s, N) \right]^{-1}, \quad j = 0, 1, \dots.$$

Sub-Poissonianity is quantified by the Fano factor F defined in Eq. (14) that naturally depends on the conditioning signal photocount number c_s . Detailed inspection [14, 29] reveals its following behavior that reflects the limited detection efficiency and the presence of dark counts in the post-selecting detector: With the increasing conditioning signal photocount number c_s , the values of Fano factor F decrease naturally first, they find their minimum and then they increase at the greater signal photocount numbers c_s that have very low probability of detection. As we are interested in the potential of the post-selection scheme to generate the most nonclassical states as possible, we further analyze the values of the Fano factor in this minimum.

With the increasing number N of grouped detection windows, the intensity of compound TWBs increases, the optimal conditioning signal photocount number c_s increases [Fig. 7(c)] and, as a consequence, the mean idler

photocount ($\langle c_{c,i} \rangle$) as well as photon ($\langle n_{c,i} \rangle$) numbers of the post-selected fields monotonously increase, as quantified in Fig. 7(a). Unfortunately, the accompanying photocount and photon-number Fano factors $F_{c_c,i}$ and $F_{n_c,i}$, respectively, also increase with the increasing number N of grouped detection windows [see Fig. 7(b)]. This increase originates in the increasing level of the overall noise in the post-selecting signal detector with the increasing number N of grouped detection windows. This noise has strong detrimental influence to the performance of the post-selection scheme. Whereas the idler field post-selected by detecting in just one detection window has around 1 photon and the Fano factor around 0.2, the idler field post-selected by the detection in 1000 grouped detection windows contains around 100 photons, but its Fano factor is only around 0.7. We note that the teeth in the curves of Fano factors F in Fig. 7(b) are caused by discrete values of the optimal conditioning signal photocount numbers c_s . The analyzed scheme for the generation of sub-Poissonian light is probabilistic and the probability p_{c_s} of success in general decreases with the number N of grouped detection windows. However, as it follows from the curve in Fig. 7(d), the probability p_{c_s} of success is in percents even for the strongest analyzed compound TWBs.

Similarly as in the case of compound TWBs, we address the non-classicality of the conditional idler fields $p_{c,i}^c$ using the NCIs based on intensity moments up to the fifth order. Relying on the results of Ref. [52], we apply the following fundamental NCIs:

$$L_{k1}^1 = \langle W^{k+1} \rangle - \langle W^k \rangle \langle W \rangle < 0, \quad k = 1, \dots, 4. \quad (32)$$

We note that the commonly used NCIs $\langle W^k \rangle - \langle W \rangle^k < 0$, $k = 2, \dots, 5$, are derived with the help of the NCIs in Eq. (32). We can see in Figs. 7(e,f) that the photocount NCDs $\tau_{L,c_c,i}$ as well as the photon NCDs $\tau_{L,n_c,i}$ gradually decrease with the increasing number N of grouped detection windows, i.e. with the increasing intensity of the post-selected idler fields. Whereas the attained values of the NCDs $\tau_{L,i}$ considerably drop down with the order of intensity moments involved in the NCIs for smaller numbers N , the values of the NCDs $\tau_{L,i}$ are close to each other for greater numbers N . In Figs. 7(e,f), the reached values of the photon NCDs $\tau_{L,n_c,i}$ are about three times greater than the values of the corresponding photocount NCDs $\tau_{L,c_c,i}$, in agreement with the detection efficiency $\eta_i = 0.33$.

We note that the models of compound TWBs detected by APDs [see Eq. (11)] and genuine TWBs detected by N -pixel PNRDs give, apart from small numbers N , very similar predictions of the quantities characterizing the post-selected sub-Poissonian fields that are in good agreement with the experimental results, as documented in the graphs of Fig. 7.

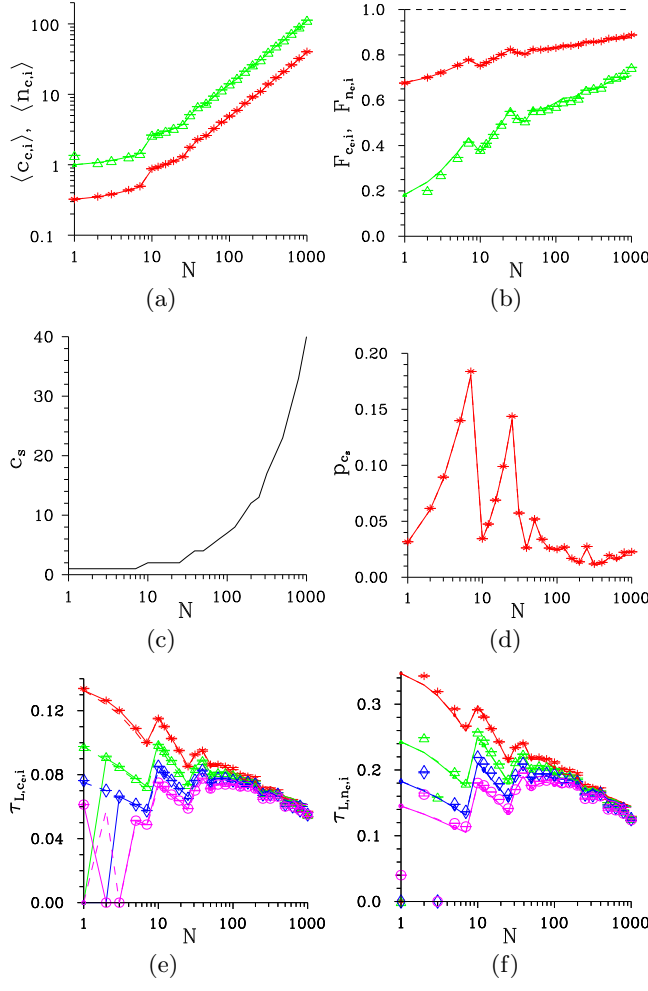


FIG. 7. (a) Mean number of idler photons $\langle n_{c,i} \rangle$ (photocounts $\langle c_{c,i} \rangle$), (b) Fano factor $F_{n_{c,i}}$ ($F_{c_{c,i}}$), (c) optimal conditioning signal photocount number c_s and (d) its probability p_{c_s} of detection and (e) [(f)] photocount [photon] number NCDs $\tau_{L,c_{c,i}}$ [$\tau_{L,n_{c,i}}$] for NCIs L_{11}^1 (red, $*$), L_{21}^1 (green, Δ), L_{31}^1 (blue, \diamond), and L_{41}^1 (magenta, \circ) belonging to conditional idler fields $p_{c,i}^c$ generated after registering the c_s optimal signal photocounts indicated in (c) and depending on the number N of grouped detection windows. In (a), (b) and (d), isolated symbols with error bars (smaller than the plotted symbols) are drawn for the experimental photocount histograms (red $*$) and fields reconstructed by the ML approach (green Δ). Experimental data plotted in (e) and (f) by isolated symbols have error bars smaller than the used symbols. Solid (dashed) curves arise in the model of compound (genuine) TWBs detected by APDs (N -pixel PNRDs). In (a), (b), (d), (e) and (f), the solid and dashed curves nearly coincide. The horizontal plain dashed line in (b) indicates the non-classicality border $F = 1$.

VII. SUB-SHOT-NOISE MEASUREMENT OF ABSORPTION

As we have seen in the previous section, post-selection with compound TWBs gives compound sub-Poissonian fields with the reduced photon-number fluctuations.

When applied to the measurement of absorption coefficients [23, 24, 30, 33, 34] they provide the sub-shot-noise precision, i.e. the precision better than the classical optimal limit reached by the coherent states with their Poissonian photon-number statistics. Below we show that the measurement precision increases with the increasing intensity of a compound TWB.

Determination of mean values $\langle c \rangle$ of photocounts is in the essence of the measurement of absorption coefficients. The mean photocount numbers $\langle c \rangle$ are measured for the fields in front and beyond the sample and their ratio gives the looked-for absorption coefficient. The precision (uncertainty) of such measurement is quantified by the relative error δc given by

$$\delta c = \frac{\sqrt{\langle (\Delta c)^2 \rangle_m}}{\langle c \rangle_m}, \quad (33)$$

and the symbol $\langle \rangle_m$ denotes averaging over the obtained finite experimental data set. If a coherent state with mean photocount number $\langle c \rangle_{cl}$ and Poissonian photocount statistics [$\langle (\Delta c)^2 \rangle_{cl} = \langle c \rangle_{cl}$] is applied N_M times, the corresponding relative error δc_{cl} takes the form:

$$\delta c_{cl} = \frac{1}{\sqrt{\langle c \rangle_{cl} N_M}}. \quad (34)$$

It serves as a reference in the definition of the normalized relative error $\delta_r c$:

$$\delta_r c = \frac{\delta c}{\delta c_{cl}}. \quad (35)$$

Sub-shot-noise measurements are characterized by $\delta_r c < 1$.

To demonstrate the ability of compound TWBs to overcome the classical limit of Eq. (34), we analyze in parallel two data sets. Speaking about the idler detector, we consider the sequence of idler detections in all detection windows as a reference. The second sequence contains the idler detections only in the detection windows in which a signal photocount was registered. If we sum the photocount numbers c_i in N subsequent detection windows in the first reference sequence, we arrive at the photocount histogram characterizing the marginal idler field of the compound TWB formed by N constituting TWBs. On the other hand, the summation of the conditioned photocount numbers $c_{c,i}$ over N subsequent detection windows in the second sequence provides us the photocount histogram of the idler field conditioned by the detection of N signal photocounts in N grouped detection windows (forming a compound TWB). This field is sub-Poissonian and overcomes the classical limit of Eq. (34).

To experimentally quantify the dependence of measurement precision on the number N_M of measurement repetitions, we determine the following experimental rel-

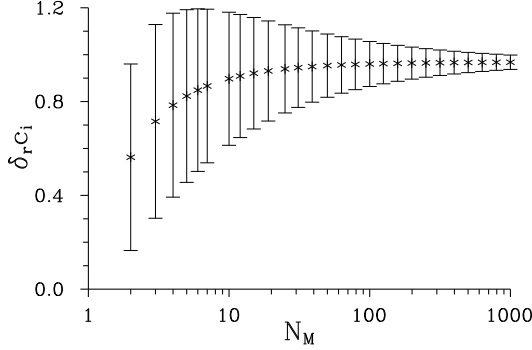


FIG. 8. Normalized relative error $\delta_r c_i$ of the idler photocount number for $N = 200$ grouped detection windows as it depends on the number N_M of measurement repetitions. The plotted relative experimental errors of $\delta_r c_i$ are given as $1/\sqrt{N_M}$.

ative error:

$$\delta c(N_M) = \left\langle \frac{\sqrt{\sum_{j=1}^{N_M} c_j^2/N_M - \left(\sum_{j=1}^{N_M} c_j/N_M\right)^2}}{\sum_{j=1}^{N_M} c_j/N_M} \right\rangle_m. \quad (36)$$

However, we have to consider sufficiently large numbers N_M of measurement repetitions to arrive at reliable (acceptable) values of the relative errors δc . We illustrate this behavior in Fig. 8, where the normalized relative error $\delta_r c_i$ of the idler photocount numbers c_i summed over $N = 200$ detection windows is plotted. The values of the normalized relative error $\delta_r c_i$ for the number N_M of measurement repetitions smaller than 10 are, though with large absolute experimental errors, artificially smaller than the correct value found for the asymptotically large numbers N_M . The data drawn in Fig. 8 suggest that the numbers N_M of measurement repetitions greater than 100 provide reliable values of the mean photocount number $\langle c_i \rangle$ for the analyzed idler field ($\langle c_i \rangle = 7.463 \pm 0.002$).

According to Eq. (34), the relative error δc decreases with the increasing field intensity, i.e. with the increasing mean photocount number $\langle c \rangle$. Working with the compound TWBs, the mean photocount numbers $\langle c \rangle$ increase linearly with the number N of grouped detection windows. These dependencies are drawn in Figs. 9(a,b) for the idler photocount numbers c_i (from the reference sequence) and conditioned idler photocount numbers $c_{c,i}$. For a given number N of grouped detection windows, the mean conditioned photocount numbers $c_{c,i}$ are about ten times greater than the mean photocount numbers c_i of the reference sequence [see Fig. 9(a)], which is given by the parameters of the post-selection scheme. On the other hand, the relative errors $\delta c_{c,i}$ belonging to the conditioned photocounts are more than $\sqrt{10}$ times smaller than the relative errors δc_i of the photocounts from the reference sequence [see Fig. 9(b)].

The reduction of the relative error $\delta c_{c,i}$ of the conditioned photocounts with respect to the relative error

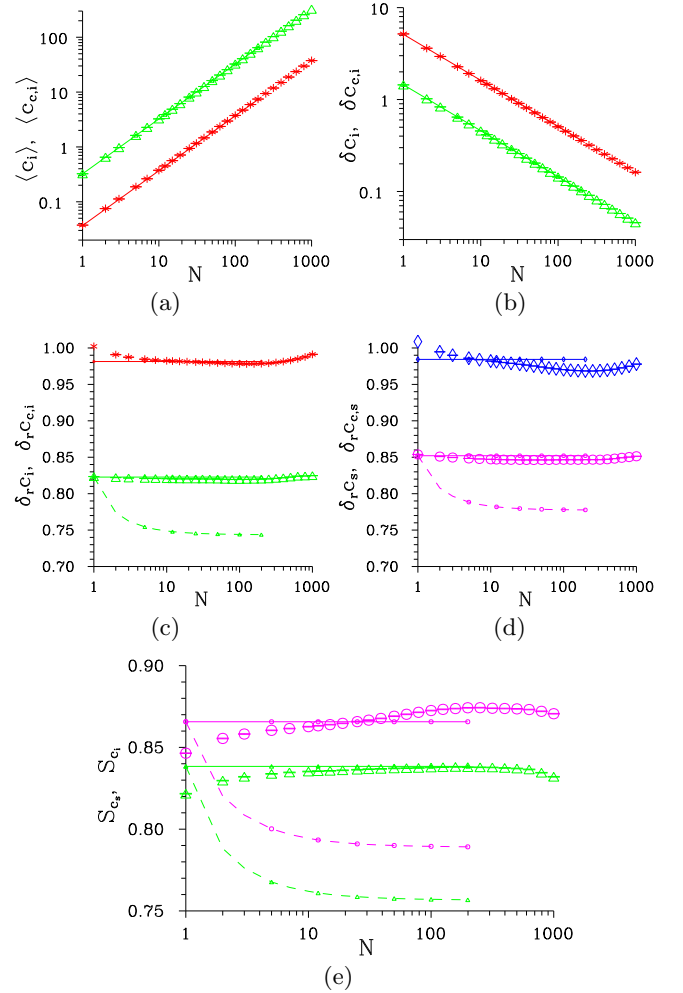


FIG. 9. (a) Mean numbers of idler photocounts $\langle c_i \rangle$ and conditioned idler photocounts $\langle c_{c,i} \rangle$ and (b) the corresponding relative errors δc_i and $\delta c_{c,i}$, (c) [(d)] normalized relative errors $\delta_r c_i$ [$\delta_r c_s$] and $\delta_r c_{c,i}$ [$\delta_r c_{c,s}$] and (e) ratios S_{c_s} and S_{c_i} of normalized relative errors as they depend on the number N of grouped detection windows. Isolated symbols with error bars (smaller than the plotted symbols) originate in the experiment with signal [idler] photocounts (blue \diamond [red $*$]) and signal [idler] conditioned photocounts (magenta \circ [green Δ]). Solid (dashed curves) are given by the model of compound (genuine) TWBs detected by APDs (N -pixel PNDRs); $N_M = 500$.

δc_i of the reference sequence by more than $\sqrt{\langle c_{c,i} \rangle/\langle c_i \rangle}$ is caused by the sub-Poissonian character of the conditioned idler photocount fields. To separate the effect of field intensity on the relative errors, we plot in Figs. 9(c,d) the idler normalized relative errors $\delta_r c_i$ and $\delta_r c_{c,i}$ together with their signal counterparts $\delta_r c_s$ and $\delta_r c_{c,s}$. The values of normalized relative errors $\delta_r c_s$ and $\delta_r c_i$ for photocounts of the reference sequence at the signal and idler detectors, respectively, are slightly below one. The multi-mode thermal character of the detected marginal signal and idler fields in the reference sequence suggests the values of these normalized relative errors

slightly above one, but the pile-up effect in the detection in individual detection windows leads to the values slightly smaller than one. On the other hand, the normalized relative errors $\delta_r c_{c,s} \approx 0.82$ and $\delta_r c_{c,i} \approx 0.85$ of the conditioned photocounts express the increased measurement precision due to the sub-Poissonian character of the conditioned photocount fields.

To quantify the improvement in the measurement precision due to the application of such compound sub-Poissonian fields, we draw in Fig. 9(e) the ratios S_{c_s} and S_{c_i} of the conditioned photocount normalized relative errors and their counterparts in the reference signal and idler sequences:

$$S_{c_a} = \frac{\delta_r c_{c,a}}{\delta_r c_a}, \quad a = s, i. \quad (37)$$

In our experiment and according to the curves in Fig. 9(e), the improvement in the measurement precision of absorption coefficient lies in the range from 12 % to 17 %. Better improvement is observed at the idler detector as the idler detection efficiency η_i is greater than the signal detection efficiency η_s . The ratios S_{c_s} and S_{c_i} slightly increase with the number N of grouped detection windows. This is caused by the increasing level of the noise with the increasing number N of grouped detection windows caused by the correlations in intra pump-pulse intensity fluctuations already discussed in relation to the Fano factors of the marginal fields and effective detection efficiencies. We note that slight decrease of the values of the ratios S_{c_s} and S_{c_i} close to $N = 1000$ in Fig. 9(e) is caused by the fact that we average over $N_M = 500$ measurement repetitions for technical reasons ($N_M < N$).

In the graphs of Fig. 9, we also plot the curves arising in the models of compound TWBs detected by APDs (solid curves) and genuine TWBs detected by N -pixel PNRDs (dashed curves). The quantities for photocount fields in the reference sequence are directly derived from the signal and idler marginal fields of compound TWBs formed by N constituting TWBs. On the other hand, the quantities for conditioned photocount fields originate in the model of sub-Poissonian fields obtained from compound TWBs formed by N constituting TWBs that are post-selected by registering N photocounts in the complementary field. According to the curves in Figs. 9(c,d,e), the use of genuine TWBs with N -pixel PNRDs instead of the analyzed compound TWBs detected in N APDs detection windows improves the measurement precision by about 50 % for $N > 10$ (signal detector: 13% \rightarrow 21%, idler detector: 16% \rightarrow 25%). This partial degradation in the measurement precision is caused by the structure of compound TWBs that, however, allows their simple detection by APDs.

We note that we have used the shot-noise limits of the applied detectors with limited detection efficiencies as a reference and beat this limit by the generated compound sub-Poissonian fields. If the detectors with detection efficiencies close to 1 are used, the analyzed experimental scheme would allow to beat the ultimate shot-noise limit

set for an ideal detector. This has been reached, e.g., in [24].

VIII. CONCLUSIONS

We have suggested a scheme for substituting genuine multi-mode twin beams by compound twin beams. The compound twin beams are composed of constituting twin beams that replace the fields in individual spatio-spectral modes of the genuine twin beams. The constituting twin beams are sufficiently weak so that they allow for the detection by single-photon sensitive on/off detectors. As a consequence the photocount statistics of compound twin beams are revealed without the need of photon-number-resolving detectors.

We have experimentally analyzed the properties of compound twin beams containing up to hundreds of photon pairs, side by side with the appropriate theoretical models. The determined marginal Fano factors, noise-reduction parameters and covariances of photon numbers revealed close similarity with the genuine twin beams. We have determined the effective detection efficiencies for the compound twin beams.

Using experimental compound twin beams with intensities varying over three orders in magnitude we have identified the non-classicality identifiers suitable for stronger twin beams and, by determining the corresponding non-classicality depths, we confirmed the highly non-classical properties of stronger compound twin beams.

Using compound twin beams and post-selection based on the photocount measurement in one beam, we have experimentally generated sub-Poissonian fields with intensities up to one hundred of photons and systematically studied their properties including non-classicality quantification. However, we have experimentally demonstrated that the real post-selection scheme loses its efficiency with the increasing field intensity.

We have experimentally demonstrated the ability of compound twin beams to perform sub-shot-noise measurements of absorption. Though the compound twin beams are less convenient than the genuine twin beams in this measurement, the use of single-photon sensitive on/off detectors in their detection represents a huge advantage, both from the point of view of their operation and high absolute detection efficiencies. Sub-shot-noise imaging with compound twin beams is especially promising for imaging of biological and other samples prone to light illumination. Broad spectra of twin beams also allow for spectroscopy measurements with sub-shot-noise precision.

ACKNOWLEDGMENTS

The authors thank GA ČR project No. 18-22102S. They also acknowledge the support from MŠMT ČR (project No. CZ.1.05/2.1.00/19.0377).

Appendix A: Model for correlated intra pump-pulse intensity fluctuations and compound twin-beam generation

The comparison of the measured effective detection efficiencies η^{eff} and the marginal photocount Fano factors F_c drawn in Figs. 5(a) and 3(b), respectively, with their theoretical counterparts shows that there occurs an additional noise that affects the compound TWBs detected in more than 100 detection windows. This additional noise is linearly proportional to the number N of detection windows for $N \geq 100$. As it affects the measured effective detection efficiencies η^{eff} , it has to be of the 'paired' origin. We attribute this noise to the correlations of the pump-pulse intensity fluctuations among subsequent pulses. These pump-pulse intensity fluctuations are transferred in the process of spontaneous parametric down-conversion into the fluctuations of integrated intensity of the paired component of a TWB (the photon-pair number). This then primarily affects the quantities directly depending on the strength of the signal and idler field correlations (the detection efficiencies η^{eff}) and secondarily the quantities depending solely on the signal or the idler field via the accompanying marginal noises.

To account for such correlations in pump-pulse intensity fluctuations in the first model of compound TWBs detected by APDs, we consider the following classical statistical Gaussian model for additional correlated intensity fluctuations $w_{p,j}$ and $w_{p,k}$ of the TWB paired components in detection windows j and k :

$$\begin{aligned} \langle w_{p,j} \rangle_w &= 0; \\ \langle w_{p,j} w_{p,k} \rangle_w &= (1 - \delta_{jk}) K \langle \mathcal{W}_p^w \rangle^2. \end{aligned} \quad (\text{A1})$$

In writing Eq. (A1), we assume that the strength of the additional intensity fluctuations $w_{p,j}$ is linearly proportional to the mean intensity $\langle \mathcal{W}_p^w \rangle$ of the TWB paired component belonging to one detection window. Provided that the detector dark-count rates can be neglected, the value of the phenomenological constant K introduced in the second relation of Eq. (A1) can be estimated by the averaged values of coefficients \bar{K}_s and \bar{K}_i drawn in Fig. 5(c).

The integrated intensity $\mathcal{W}_p^{\text{all}}$ of the paired component of a compound TWB originating in N grouped detection windows and involving the additional intensity fluctuations is determined as $\mathcal{W}_p^{\text{all}} \equiv \mathcal{W}_p + \sum_{j=1}^N w_{p,j}$. Its moments with respect to the additional pump-pulse in-

tensity fluctuations take the form:

$$\begin{aligned} \langle \mathcal{W}_p^{\text{all}} \rangle_w &= \langle \mathcal{W}_p \rangle, \\ \langle [\mathcal{W}_p^{\text{all}}]^2 \rangle_w &= \langle \mathcal{W}_p^2 \rangle + K N (N - 1) \langle \mathcal{W}_p^w \rangle^2. \end{aligned} \quad (\text{A2})$$

The original formula (19) for the signal effective detection efficiency η_s^{eff} is then modified into the form

$$\eta_s^{\text{eff}} = \eta_s \frac{\langle \mathcal{W}_p \rangle + \langle (\Delta \mathcal{W}_p)^2 \rangle + K N (N - 1) \langle \mathcal{W}_p^w \rangle^2}{\langle \mathcal{W}_p \rangle + \langle \mathcal{W}_i \rangle}. \quad (\text{A3})$$

Similarly, the signal photocount Fano factor $F_{c,s}$ defined in Eq. (14) is expressed in this model as follows:

$$\begin{aligned} F_{c,s} &= 1 + \eta_s \left[\langle (\Delta \mathcal{W}_p)^2 \rangle + \langle (\Delta \mathcal{W}_s)^2 \rangle \right. \\ &\quad \left. + K N (N - 1) \langle \mathcal{W}_p^w \rangle^2 \right] \left[\langle \mathcal{W}_p \rangle + \langle \mathcal{W}_s \rangle \right]^{-1}. \end{aligned} \quad (\text{A4})$$

Also, the formula (15) for the noise-reduction-parameter R_c of photocounts can be appropriately modified:

$$\begin{aligned} R_c &= 1 + \left[(\eta_s - \eta_i)^2 \left[\langle (\Delta \mathcal{W}_p)^2 \rangle + K N (N - 1) \langle \mathcal{W}_p^w \rangle^2 \right] \right. \\ &\quad \left. - 2 \eta_s \eta_i \langle \mathcal{W}_p \rangle + \eta_s^2 \langle (\Delta \mathcal{W}_s)^2 \rangle + \eta_i^2 \langle (\Delta \mathcal{W}_i)^2 \rangle \right] \\ &\quad \times \left[(\eta_s + \eta_i) \langle \mathcal{W}_p \rangle + \eta_s \langle \mathcal{W}_s \rangle + \eta_i \langle \mathcal{W}_i \rangle \right]^{-1}. \end{aligned} \quad (\text{A5})$$

We note that the corresponding quantities characterizing photon-number fields are also given by formulas (A4) and (A5) in which we set $\eta_s = \eta_i = 1$.

The Fano factors $F_{c,i}$ and $F_{n,i}$ and the effective detection efficiencies η_s^{eff} and η_i^{eff} , that show greater declinations between the experimental data and predictions of the original model without the correlations in pump-pulse intensity fluctuations for greater numbers N of grouped detection windows, are plotted in Fig. 3(b) and Fig. 5(a), respectively. The solid plain curves close to the experimental points in Figs. 3(b) and 5(a) drawn for the model with correlations in intra pump-pulse intensity fluctuations and $K \langle \mathcal{W}_p^w \rangle^2 = 1 \times 10^{-5}$ describe well the behavior of the studied quantities for great numbers N of grouped detection windows. We have in the model $\langle \mathcal{W}_p^w \rangle = m_p b_p = 0.10185$ and so $K = 0.965 \times 10^{-3}$, in accordance with the values of coefficients \bar{K}_s and \bar{K}_i plotted in Fig. 5(c). As it follows from Eq. (A5), the correlations in pump-pulse intensity fluctuations influence only weakly the values of noise-reduction-parameters R_c and R_n in our case in which $\eta_s \approx \eta_i$. We note that, in our opinion, the slightly larger theoretical values of effective detection efficiencies η_s^{eff} and η_i^{eff} in Fig. 5(a) in the area around $N = 100$ indicate longer-range death-time effects in the response of the used APDs and processing electronics [53].

[1] R. J. McIntyre, "Theory of microplasma instability in silicon," *J. Appl. Phys.* **32**, 983–995 (1961).

[2] L. Mandel and E. Wolf, *Optical Coherence and Quantum Optics* (Cambridge Univ. Press, Cambridge, 1995).

- [3] J. Peřina, *Quantum Statistics of Linear and Nonlinear Optical Phenomena* (Kluwer, Dordrecht, 1991).
- [4] H. Paul, P. Törmä, T. Kiss, and I. Jex, “Photon chopping: New way to measure the quantum state of light,” *Phys. Rev. Lett.* **76**, 2464–2467 (1996).
- [5] D. Achilles, Ch. Silberhorn, C. Sliwa, K. Banaszek, and I. A. Walmsley, “Fiber-assisted detection with photon number resolution,” *Opt. Lett.* **28**, 2387 (2003).
- [6] M. J. Fitch, B. C. Jacobs, T. B. Pittman, and J. D. Franson, “Photon-number resolution using time-multiplexed single-photon detectors,” *Phys. Rev. A* **68**, 043814 (2003).
- [7] O. Haderka, M. Hamar, and J. Peřina Jr., “Experimental multi-photon-resolving detector using a single avalanche photodiode,” *Eur. Phys. J. D* **28**, 149–154 (2004).
- [8] O. Haderka, J. Peřina Jr., M. Hamar, and J. Peřina, “Direct measurement and reconstruction of nonclassical features of twin beams generated in spontaneous parametric down-conversion,” *Phys. Rev. A* **71**, 033815 (2005).
- [9] J. Peřina Jr., M. Hamar, V. Michálek, and O. Haderka, “Photon-number distributions of twin beams generated in spontaneous parametric down-conversion and measured by an intensified CCD camera,” *Phys. Rev. A* **85**, 023816 (2012).
- [10] G. Chesi, L. Malinverno, A. Allevi, R. Santoro, M. Caccia, and M. Bondani, “Measuring nonclassicality with silicon photomultipliers,” *Opt. Lett.* **44**, 1371–1374 (2019).
- [11] G. Harder, T. J. Bartley, A. E. Lita, S. W. Nam, T. Gerrits, and C. Silberhorn, “Single-mode parametric-down-conversion states with 50 photons as a source for mesoscopic quantum optics,” *Phys. Rev. Lett.* **116**, 143601 (2016).
- [12] O. S. Magaña-Loaiza, R. de J. León-Montiel, A. Pérez-Leija, A. B. URen, C. You, K. Busch, A. E. Lita, S. W. Nam, R. P. Mirin, and T. Gerrits, “Multiphoton quantum-state engineering using conditional measurements,” *npj Quant. Inf.* **5**, 80 (2019).
- [13] A. J. Miller, S. W. Nam, J. M. Martinis, and A. V. Sergienko, “Demonstration of a low-noise near-infrared photon counter with multiphoton discrimination,” *Appl. Phys. Lett.* **83**, 791–793 (2003).
- [14] J. Peřina Jr., V. Michálek, and O. Haderka, “Higher-order sub-Poissonian-like nonclassical fields: Theoretical and experimental comparison,” *Phys. Rev. A* **96**, 033852 (2017).
- [15] I. A. Malkin and V. I. Manko, *Dynamical symmetries and coherent states of quantum systems* (Nauka, Moscow, 1979).
- [16] Ch. C. Gerry and E. E. Hach III, “Generation of even and odd coherent states in a competitive two-photon process,” *Phys. Lett. A* **174**, 185–189 (1993).
- [17] S. Friberg, C. K. Hong, and L. Mandel, “Measurement of time delays in the parametric production of photon pairs,” *Phys. Rev. Lett.* **54**, 2011–2013 (1985).
- [18] D. N. Klyshko, “Use of two-photon light for absolute calibration of photoelectric detectors,” *Kvantovaya Elektron. (Moscow)* **7**, 1932–1940 (1980).
- [19] A. Migdall, “Correlated-photon metrology without absolute standards,” *Physics Today* **52**, 41–46 (1999).
- [20] G. Brida, I. P. Degiovanni, M. Genovese, M. L. Rastello, and I. R. Berchera, “Detection of multimode spatial correlation in PDC and application to the absolute calibration of a CCD camera,” *Opt. Express* **18**, 20572–20584 (2010).
- [21] J. Peřina Jr., O. Haderka, A. Allevi, and M. Bondani, “Absolute calibration of photon-number-resolving detectors with an analog output using twin beams,” *Appl. Phys. Lett.* **104**, 041113 (2014).
- [22] G. Brida, M. Genovese, and I. R. Berchera, “Experimental realization of sub-shot-noise quantum imaging,” *Nat. Phys.* **4**, 227–230 (2010).
- [23] M. Genovese, “Real applications of quantum imaging,” *J. Opt.* **18**, 073002 (2016).
- [24] E. Losero, I. Ruo-Berchera, A. Meda, A. Avella, and M. Genovese, “Unbiased estimation of an optical loss at the ultimate quantum limit with twin-beams,” *Sci. Rep.* **8**, 7431 (2018).
- [25] B. E. A. Saleh and M. C. Teich, “Can the channel capacity of a light-wave communication system be increased by the use of photon-number-squeezed light?” *Phys. Rev. Lett.* **58**, 2656–2659 (1987).
- [26] I. Straka, L. Lachman, J. Hloušek, M. Miková, M. Mičuda, M. Ježek, and R. Filip, “Quantum non-Gaussian multiphoton light,” *npj Quant. Inf.* **4**, 4 (2018).
- [27] J. G. Rarity, P. R. Tapster, and E. Jakeman, “Observation of sub-Poissonian light in parametric downconversion,” *Opt. Commun.* **62**, 201–206 (1987).
- [28] J. Laurat, T. Coudreau, N. Treps, A. Maitre, and C. Fabre, “Conditional preparation of a quantum state in the continuous variable regime: Generation of a sub-Poissonian state from twin beams,” *Phys. Rev. Lett.* **91**, 213601 (2003).
- [29] J. Peřina Jr., O. Haderka, and V. Michálek, “Sub-Poissonian-light generation by postselection from twin beams,” *Opt. Express* **21**, 19387–19394 (2013).
- [30] E. Jakeman and J. G. Rarity, “The use of pair production processes to reduce quantum noise in transmission measurements,” *Opt. Commun.* **59**, 219–223 (1986).
- [31] V. Giovannetti, S. Lloyd, and L. Maccone, “Quantum metrology,” *Phys. Rev. Lett.* **96**, 010401 (2006).
- [32] M. Li, C.-L. Zou, D. Liu, G.-P. Guo, G.-C. Guo, and X.-F. Ren, “Enhanced absorption microscopy with correlated photon pairs,” *Phys. Rev. A* **98**, 012121 (2018).
- [33] J. Sabines-Chesterkind, A. R. McMillan, P. A. Moreau, S. K. Joshi, S. Knauer, E. Johnston, J. G. Rarity, and J. C. F. Matthews, “Twin-beam sub-shot-noise raster-scanning microscope,” *Opt. Express* **27**, 30810–30818 (2019).
- [34] R. Whittaker, C. Erven, A. Neville, M. Berry, J. L. OBrien, H. Cable, and J. C. F. Matthews, “Absorption spectroscopy at the ultimate quantum limit from single-photon states,” *New J. Phys.* **19**, 023013 (2017).
- [35] J. Peřina Jr., O. Haderka, V. Michálek, and M. Hamar, “State reconstruction of a multimode twin beam using photodetection,” *Phys. Rev. A* **87**, 022108 (2013).
- [36] A. P. Dempster, N. M. Laird, and D. B. Rubin, “Maximum likelihood from incomplete data via the EM algorithm,” *J. R. Statist. Soc. B* **39**, 1–38 (1977).
- [37] Y. Vardi and D. Lee, “From image deblurring to optimal investments: Maximum likelihood solutions for positive linear inverse problems,” *J. R. Statist. Soc. B* **55**, 569–612 (1993).
- [38] P. M. Morse and H. Feshbach, *Methods of Theoretical Physics, Vol. 1* (McGraw–Hill, Amsterdam, 1953).
- [39] J. Peřina Jr., O. Haderka, M. Hamar, and V. Michálek, “Absolute detector calibration using twin beams,” *Opt. Lett.* **37**, 2475–2477 (2012).

[40] O. Jedrkiewicz, Y. K. Jiang, E. Brambilla, A. Gatti, M. Bache, L. A. Lugiato, and P. Di Trapani, “Detection of sub-shot-noise spatial correlation in high-gain parametric down-conversion,” *Phys. Rev. Lett.* **93**, 243601 (2004).

[41] M. Bondani, A. Allevi, G. Zambra, M. G. A. Paris, and A. Andreoni, “Sub-shot-noise photon-number correlation in a mesoscopic twin beam of light,” *Phys. Rev. A* **76**, 013833 (2007).

[42] J.-L. Blanchet, F. Devaux, L. Furfaro, and E. Lantz, “Measurement of sub-shot-noise correlations of spatial fluctuations in the photon-counting regime,” *Phys. Rev. Lett.* **101**, 233604 (2008).

[43] G. Brida, L. Caspani, A. Gatti, M. Genovese, A. Meda, and I. R. Berchera, “Measurement of sub-shot-noise spatial correlations without background subtraction,” *Phys. Rev. Lett.* **102**, 213602 (2009).

[44] J. Peřina Jr., I. I. Arkhipov, V. Michálek, and O. Haderka, “Non-classicality and entanglement criteria for bipartite optical fields characterized by quadratic detectors,” *Phys. Rev. A* **96**, 043845 (2017).

[45] J. Peřina Jr., O. Haderka, and V. Michálek, “Non-classicality and entanglement criteria for bipartite optical fields characterized by quadratic detectors II: Criteria based on probabilities,” *Phys. Rev. A* **102**, 043713 (2020).

[46] I. S. Gradshteyn and I. M. Ryzhik, *Table of Integrals, Series, and Products*, 6th ed. (Academic Press, San Diego, 2000).

[47] C. T. Lee, “Measure of the nonclassicality of nonclassical states,” *Phys. Rev. A* **44**, R2775—R2778 (1991).

[48] J. M. Raimond, M. Brune, and S. Haroche, “Manipulating quantum entanglement with atoms and photons in a cavity,” *Rev. Mod. Phys.* **73**, 565—583 (2001).

[49] H. Zou, S. Zhai, J. Guo, R. Yang, and J. Gao, “Preparation and measurement of tunable highpower sub-Poissonian light using twin beams,” *Opt. Lett.* **31**, 1735—1737 (2006).

[50] M. Lamperti, A. Allevi, M. Bondani, R. Machulka, V. Michálek, O. Haderka, and J. Peřina Jr., “Optimal sub-Poissonian light generation from twin beams by photon-number resolving detectors,” *J. Opt. Soc. Am. B* **31**, 20—25 (2014).

[51] T. S. Iskhakov, V. C. Usenko, U. L. Andersen, R. Filip, M. V. Chekhova, and G. Leuchs, “Heralded source of bright multi-mode mesoscopic sub-Poissonian light,” *Opt. Lett.* **41**, 2149—2152 (2016).

[52] J. Peřina Jr., V. Michálek, and O. Haderka, “Non-classicality of optical fields as observed in photocount and photon-number distributions,” *Opt. Express* **28**, 32620—32631 (2020).

[53] I. Straka, J. Grygar, J. Hloušek, and M. Ježek, “Counting statistics of actively quenched SPADs under continuous illumination,” *J. Lightwave Tech.* **38**, 4765—4771 (2020).